Global Biogeochemical Cycles

Contrasting Upper and Deep Ocean Oxygen Response to Protracted Global Warming

T. L. Frölicher[1,2] , M. T. Aschwanden[1,2,3], N. Gruber[3] , S. L. Jaccard[2,4] , J. P. Dunne[5] , and D. Paynter[5]

[1]Climate and Environmental Physics, Physics Institute, University of Bern, Bern, Switzerland, [2]Oeschger Centre for Climate Change Research, University of Bern, Bern, Switzerland, [3]Environmental Physics, Institute of Biogeochemistry and Pollutant Dynamics, Zürich, Switzerland, [4]Institute of Geological Sciences, University of Bern, Bern, Switzerland, [5]NOAA/OAR Geophysical Fluid Dynamics Laboratory, Princeton, NJ, USA

Abstract It is well established that the ocean is currently losing dissolved oxygen (O_2) in response to ocean warming, but the long-term, equilibrium response of O_2 to a warmer climate is neither well quantified nor understood. Here we use idealized multimillennial global warming simulations with a comprehensive Earth system model to show that the equilibrium response in ocean O_2 differs fundamentally from the ongoing transient response. After physical equilibration of the model (>4,000 years) under a two times preindustrial CO_2 scenario, the deep ocean is better ventilated and oxygenated compared to preindustrial conditions, even though the deep ocean is substantially warmer. The recovery and overshoot of deep convection in the Weddell Sea and especially the Ross Sea after ~720 years causes a strong increase in deep ocean O_2 that overcompensates the solubility-driven decrease in O_2. In contrast, O_2 in most of the upper tropical ocean is substantially depleted owing to the warming-induced O_2 decrease dominating over changes in ventilation and biology. Our results emphasize the millennial-scale impact of global warming on marine life, with some impacts emerging many centuries or even millennia after atmospheric CO_2 has stabilized.

1. Introduction

Dissolved oxygen (O_2) is of fundamental importance for essentially all higher forms of marine life (Bindoff et al., 2019; Pörtner et al., 2014). Observation-based estimates show that the ocean O_2 inventory has decreased by about 0.5% to 3.3% over the 1970–2010 period (Bindoff et al., 2019; Helm et al., 2011; Ito et al., 2017; Schmidtko et al., 2017) and that the volume of O_2-depleted waters in the oxygen minimum zones (OMZs) has expanded by about 3% to 8% (Bindoff et al., 2019; Stramma et al., 2008). Earth system model (ESM) projections consistently suggest that the global ocean O_2 content will continue to decrease during the 21st century (e.g., Bopp et al., 2013; Frölicher et al., 2009; Matear et al., 2000; Plattner et al., 2002; Sarmiento et al., 1998) but with some substantial regional differences, especially in the OMZs. While most model simulations suggest their continued expansion, a few models also suggest their shrinkage (Bopp et al., 2013; Cocco et al., 2013; Gnanadesikan et al., 2012). Decreases in O_2 levels below certain physiological thresholds, as projected under global warming, will have deleterious consequences for marine organisms and ecosystems (Deutsch et al., 2015; Stramma et al., 2011; Vaquer-Sunyer & Duarte, 2008) and affect the cycling of carbon and nutrients, potentially amplifying global warming (Keeling et al., 2010).

Global warming is the main driver of open ocean deoxygenation, but it acts in two different ways. First, the solubility of O_2 decreases in warmer waters (Garcia & Gordon, 1992). Second, the warming of the upper ocean combined with the climate change-induced freshening of the subpolar regions leads to a general strengthening of upper ocean stratification (Collins et al., 2013; Manabe et al., 1991; Sarmiento et al., 1998). This reduces the downward supply of O_2-rich surface waters (Breitburg et al., 2018; Keeling et al., 2010; Levin, 2018; Oschlies et al., 2018), depleting O_2 in the ocean's interior. The contribution of changes in the biological consumption of O_2 in the ocean's interior tends to differ between the low latitudes, where the enhanced upper ocean stratification reduces the resupply of nutrients to the productive surface ocean curtailing primary and export production (Laufkötter et al., 2015, 2016; Steinacher et al., 2010), and the high latitudes where most models predict an increase in export and hence O_2 consumption at depth. These three aspects reinforce each other in the temperate to high latitudes, leading to very consistently projected

decreases in O_2 under transient global warming. In the upper ocean of the low latitudes, the changes in ventilation/biology and O_2 solubility tend to compensate each other, resulting in smaller projected O_2 decreases (Bopp et al., 2017; Gnanadesikan et al., 2012) or even increases.

Only a few studies have documented ocean O_2 changes beyond 2100. Recently, Fu et al. (2018) suggested that the current trend of gradually declining O_2 levels in the tropical thermocline may reverse after 2100, resulting in shrinking volumes of the OMZs through the end of their simulation in the Year 2300. They attributed this potential reoxygenation of the tropical ocean thermocline to intensified ventilation that kicked in their simulation after 2150 and to a decline in tropical export production leading to reduced biological O_2 consumption in the underlying thermocline. In the deep ocean, several studies suggested a recovery of deep ocean O_2 levels under multimillennial global warming scenarios (Battaglia & Joos, 2018; Ridgwell & Schmidt, 2010; Schmittner et al., 2008; Yamamoto et al., 2015). In all of these models, the recovery was caused by a millennial-scale emergence of a more vigorous deep ocean ventilation under protracted global warming. However, all but one of these studies were conducted with reduced complexity models that have no dynamic atmosphere or employ an ocean model with very coarse ocean resolution. This is primarily a consequence of comprehensive ESMs generally being too expensive to run for millennia. And the one exception, that is, the study by Yamamoto et al. (2015), employed an offline approach with circulation fields from a CMIP3-class climate model. It is thus imperative to revisit the deep ocean reoxygenation with a state-of-the-art ESM of the CMIP5 class and to investigate also the development of O_2 in the upper ocean, especially in the tropical thermocline. There, the evolution of the O_2-depleted water masses depends on the subtle balance between changes in O_2-solubility and ocean ventilation (including O_2 consumption) (Fu et al., 2018; Ito & Deutsch, 2013). It remains, therefore, unclear whether these typically opposing processes in the low latitudes will evolve simultaneously on multimillennial timescales, when the climate system approaches a new equilibrium under elevated atmospheric CO_2 concentrations.

Here we use millennial-scale simulations of a comprehensive ESM under an idealized global warming scenario to show that the deep ocean becomes better ventilated and oxygenated and that, conversely, the (sub) tropical shallow subsurface ocean is projected to lose O_2 in an equilibrated warm climate.

2. Methods

2.1. GFDL-ESM2M

The Geophysical Fluid Dynamics Laboratory (GFDL)-ESM2M is a comprehensive global ESM developed at the GFDL (Dunne et al., 2012, 2013). The GFDL-ESM2M consists of atmosphere, ocean, sea ice, and land modules including biogeochemistry. The ocean component of the GFDL-ESM2M is the Modular Ocean Model version 4p1 (MOM4p1; Griffies, 2012), with a nominal 1° horizontal resolution with higher resolution near the equator and 50 unevenly spaced vertical depth levels. Ocean mesoscale eddies are not explicitly resolved but are parameterized using the GM-Redi schemes (Griffies, 1998). The atmospheric module (AM2; Anderson et al., 2004) has a horizontal resolution of 2° latitude × 2.5° longitude and 24 vertical levels. In contrast to earlier multimillennial simulations focusing on oceanic O_2 and using models of intermediate complexity (Battaglia & Joos, 2018; Schmittner et al., 2008), the GFDL-ESM2M includes changes in the hydrological cycle, cloud cover, wind fields, and sea ice (Winton, 2000). Similar to other CMIP5-type ESMs, the GFDL-ESM2M lacks a land ice sheet model and, therefore, freshwater fluxes from the Greenland and Antarctic ice sheets as well as mountain glaciers.

The ocean biogeochemical and ecological component is version two of the Tracers of Ocean Productivity with Allometric Zooplankton (TOPAZv2) module that parameterizes the cycling of carbon, nitrogen, phosphorus, silicon, iron, oxygen, alkalinity, and lithogenic material as well as surface sediment calcite (Dunne et al., 2013). TOPAZv2 includes three explicit phytoplankton groups, namely, small and large phytoplankton as well as diazotrophs, and one implicit zooplankton group. A fraction of the sinking organic material is associated with denser ballast material (biogenic opal, calcium carbonate, and lithogenic material) and remineralizes only when these materials dissolve. At well oxygenated conditions, the unprotected fraction is remineralized with a constant depth scale of 188 m. Remineralization is slower at low O_2 and suppressed in the absence of O_2 (<1 μmol kg^{-1}) (Gnanadesikan et al., 2012). The remineralization and sinking speed of organic material is insensitive to temperature.
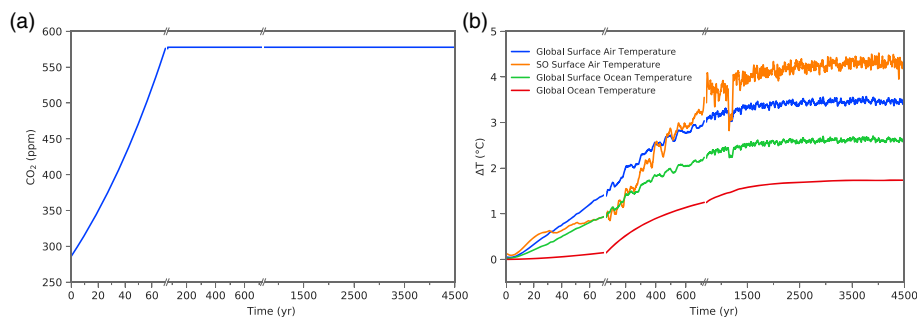
Figure 1. (a) Prescribed global annual mean atmospheric CO_2 concentration. (b) Simulated global annual mean surface air (blue line), Southern Ocean surface air (orange), global surface ocean (green), and mean ocean (red) temperature anomalies relative to first 5 years of the simulation. The time series in (b) have been smoothed with a Savitzky-Golay filter with a window size of 51 years (Savitzky & Golay, 1964). Note that the x axis is discontinuous, with finer temporal resolution of the first 70 and 720 years.

The GFDL-ESM2M simulates the large-scale physical (Dunne et al., 2012) and biogeochemical (Dunne et al., 2013) patterns with competitive fidelity among the CMIP5 suite of models (Bopp et al., 2013). Analyzing a 1,500 year preindustrial control simulation (see section 2.2), the model reproduces observation-based estimates of the formation and circulation of North Atlantic Deep Water (Dunne et al., 2012). But the model forms Antarctic Bottom Water by open ocean convection (Heuzé et al., 2013), while in reality bottom water is generally formed as dense water spills off the Antarctic continental shelf. This feature is a common bias in current ESMs, whose implications will be discussed in our caveat section below. The simulated spatial distribution of O_2 matches the observations well, both in the upper and the deeper ocean (supporting information Figure S1). The mean O_2 concentration simulated by the GFDL-ESM2M in the upper (sub)tropical ocean (30°S–30°N) between 200 and 1,000 m of 95 mmol m^{-3} is somewhat lower than the observed concentration of 113 mmol m^{-3}. This negative bias in O_2 is also reflected in the volume of O_2 depleted waters. For a threshold of 20 mmol m^{-3}, the volume of O_2-depleted waters in GFDL-ESM2M is by a factor of 3.8 higher than the observational-based estimate (Bianchi et al., 2012; Fu et al., 2018). In the global deep ocean below 2,000 m, the model simulates also a slightly lower O_2 concentrations of 174 mmol m^{-3} compared to observations (189 mmol m^{-3}), with most of the negative bias located in the eastern Pacific and Atlantic (supporting information Figure S1b). Also taking into account previous assessments of simulated O_2 by the GFDL-ESM2M (Bopp et al., 2013; Cabré et al., 2015; Dunne et al., 2013; Fu et al., 2018; Gnanadesikan et al., 2012), we conclude that the model performs relatively well against some key performance metrics and, therefore, appears to be adequate to assess changes in open ocean oxygen on multicentennial to millennial timescales.

2.2. Multimillennial Global Warming Simulation

We analyze an idealized 4,500 year-long CO_2 doubling simulation (Paynter et al., 2018) initialized from a multimillennial 1860 preindustrial simulation, wherein atmospheric CO_2 was held fixed at 287.1 ppm. From this value, atmospheric CO_2 was then prescribed to increase by 1% per year during a period of 70 years until it reached a CO_2 doubling (574.2 ppm). Thereafter, atmospheric CO_2 is kept fixed (Figure 1a). All radiative forcing agents other than CO_2 were kept constant at their preindustrial levels. We also performed a second ensemble member for the period ranging from Years 673 to 822 branching off the first ensemble simulation to assess whether the onset of the deepwater formation in the Ross Sea was stochastically driven. In addition, an accompanying control simulation with constant preindustrial radiative forcing was run for the first 1,500 years in order to determine the influence of model drift.

The general climate response of the GFDL-ESM2M to a doubling of atmospheric CO_2 is described in detail elsewhere (Paynter et al., 2018; Rugenstein et al., 2020). Here we nonetheless provide a brief summary of the most important physical characteristics. During the first 70 years (average period 61 to 80 years), the global mean surface air temperature increases by 1.3°C (blue line in Figure 1b). This transient climate response is at the lower end of the CMIP5 model range of 1.1°C to 2.5°C (Forster et al., 2013). The initial rate of surface air

temperature increase poleward of 55°S is slow, as it is dampened by the large heat capacity of the ocean and the continuing Southern Ocean heat uptake, but maintains a higher warming rate than the global mean after CO_2 is stabilized in Year 70 and is abruptly increased by an additional 0.7°C around Year 720 (orange line in Figure 1b). The equilibrium temperature response of 3.4°C to a doubling of atmospheric CO_2 is similar to the CMIP5 multimodel mean of 3.2°C (Forster et al., 2013) and to the last deglacial global average temperature change (Shakun et al., 2012). The physical model can be considered to be in equilibrium with the elevated radiative forcing at the end of the 4,500 year simulation, that is, the global ocean heat uptake is virtually zero (-0.07 Wm^{-2} averaged over last 200 years of the simulation; Paynter et al., 2018). The surface ocean temperature change equilibrates at 2.6°C (green line in Figure 1b) and the global ocean temperature change at 1.7°C (red line in Figure 1b).

2.3. Analysis

To assess changes in ocean O_2, we decompose the total changes in oxygen ($\Delta O_2 = [O_2] - [O_{2,pi}]$, with $O_{2,pi}$ representing the O_2 concentration averaged over the first 5 years of the transient global warming simulation) into a solubility component (ΔO_2^{sol}), a disequilibrium component (ΔO_2^{diseq}), and a combined circulation and remineralization ($\Delta O_2^{circ/rem}$) component following Frölicher et al. (2009):

$$\Delta O_2 = \Delta O_2^{sol} + \Delta O_2^{circ/rem} + \Delta O_2^{diseq}. \tag{1}$$

ΔO_2^{sol} is determined by the O_2 solubility in seawater, which is a function of ocean temperature and to a lesser extent salinity (Garcia & Gordon, 1992). Warming and salinification of the ocean decreases the solubility and therefore ΔO_2^{sol}. The term $\Delta O_2^{circ/rem}$ reflects changes in organic matter remineralization and physical O_2 supply by the large-scale ocean circulation and mixing. A decrease in biological export production would lead to an increase in $\Delta O_2^{circ/rem}$ owing to reduced O_2 demand from remineralization. In contrast, a decrease in ventilation (increase in stratification) would lead to a decrease in $\Delta O_2^{circ/rem}$, as the longer residence time increases cumulative O_2 demand in subsurface waters. ΔO_2^{diseq} is the disequilibrium of the surface ocean O_2 with respect to the atmospheric O_2 concentration, as surface ocean O_2 is usually not at saturation. In most of the low-latitude surface ocean, O_2 is slightly supersaturated due to photosynthesis and sluggish ventilation. In the high latitudes surface waters, in particular in regions where convection occurs, O_2 can be undersaturated due to rapid heat loss and mixing of O_2-depleted deep waters to the surface (Ito et al., 2004). In this study, O_2^{diseq} is included in $\Delta O_2^{circ/rem/diseq}$:

$$\Delta O_2 \approx \Delta O_2^{sol} + \Delta O_2^{circ/rem/diseq}. \tag{2}$$

$\Delta O_2^{circ/rem/diseq}$ can therefore be calculated as the difference between ΔO_2 and ΔO_2^{sol}. We also estimate the ventilation time and the organic matter respiration. For the ventilation time, we use an ideal age tracer, which is set to zero in the surface ocean and ages at a rate 1 year year^{-1} below that (Thiele & Sarmiento, 1990). We use the changes in the export production of particulate organic matter at 100 m depth as a proxy for organic matter remineralization at subsurface. A quantitative analysis of all O_2 transport terms, as has been done previously (Gnanadesikan et al., 2012), is not possible, because of a lack of diagnostics in these multimillennial simulations.

We calculate the Atlantic meridional overturning circulation (AMOC) and the Southern Ocean meridional overturning circulation (SMOC) as the vertically and zonally integrated meridional transport in the Atlantic basin and in the Southern Ocean, respectively:

$$\psi(y, z) = \int_z^\eta \int_{x_w}^{x_e} v \, dx \, dz, \tag{3}$$

where v is the meridional velocity expressed as the sum of resolved and parameterized mesoscale and submesoscale processes (Griffies, 2012), x is the zonal coordinate (increasing eastward), z is the vertical coordinate (increasing upward), η is the ocean free surface, and x_w and x_e are the westward and eastward boundaries of the North Atlantic basin or the Southern Ocean region. We report the strength of the AMOC and SMOC as the annual mean below 500 m of the vertical maximum north of 20°N for the AMOC and the minimum south of 60°S for the SMOC.

We assess the effect of ocean-atmosphere interactions on surface density changes by calculating the sum of the thermal ($F_{\rho,thermal}$) and haline ($F_{\rho,haline}$) density fluxes according to Liu et al. (2017):

$$F_\rho = F_{\rho,\,thermal} + F_{\rho,\,haline} = -\alpha \cdot \frac{Q}{c_p} + \rho(0, SST) \cdot \beta \cdot \frac{(E - P - R - I) \cdot SSS}{1 - SSS}, \tag{4}$$

where α and β are the thermal expansion and haline contraction coefficients, respectively. SST is the sea surface temperature and SSS the sea surface salinity. Q denotes the net heat flux from the atmosphere into the ocean, c_p the specific heat capacity of seawater, $\rho(0, SST)$ is the density of freshwater with salinity of 0 and temperature of SST, and E, P, R, and I the freshwater flux from evaporation, precipitation, river run-off, and sea ice melt, respectively.

To investigate changes in the stability of the water column (i.e., stratification), we calculate the squared Brunt-Väisälä frequency (N^2; Talley et al. (2011)):

$$N^2(\rho) = -\frac{g}{\rho}\frac{d\rho}{dz}, \tag{5}$$

where g it the local acceleration of gravity, ρ the in situ density, and $d\rho/dz$ the vertical gradient of the in situ density. To assess whether stability changes are caused by salinity or temperature changes, we also determine N^2 based on the density with either the temperature ($N^2(\rho_{T0,S})$) or the salinity ($N^2(\rho_{T,S0})$) prescribed to preindustrial (0) values.

For all analyses, we use the model output as is, that is, we do not correct the output with the results from the preindustrial control simulation. However, we generally illustrate the corresponding preindustrial control simulation to indicate potential drift.

3. Results

3.1. Global Ocean Oxygen Changes

The multimillennial response of the global oceanic O_2 content to changes in atmospheric CO_2 and associated global warming is characterized by three phases (Figure 2a). Phase I covers Years 1–70 and is characterized by steadily increasing atmospheric CO_2 and globally decreasing O_2 levels; phase II encompasses Years 71–720 and is characterized by constant atmospheric CO_2 levels, yet global O_2 levels continue to decline; phase III covers Years 721–4500 and is marked by constant atmospheric CO_2 and a gradually recovering global O_2 inventory.

During phase I, under steadily increasing atmospheric CO_2 forcing, the global oceanic O_2 inventory decreases by −3.6 Pmol (−1.6%; black line in Figure 2a). After the CO_2 forcing has stabilized during phase II, the global O_2 inventory further decreases such that the O_2 content is 17.5 Pmol (−7.8%) smaller by Year 720 than at the beginning of the simulation. The warming-induced reduction in solubility, O_2^{sol}, accounts for 40% of the total decrease by the end of phase I, amounting 68% of the total O_2 loss by the end of phase II (blue line in Figure 2a). The additional O_2 loss results from changes in ocean circulation and organic matter respiration as indicated by the decrease in $O_2^{circ/rem/diseq}$ (orange line in Figure 2a). The relative contribution of O_2^{sol} to the total change during phase I is consistent with earlier multimodel studies, which reported that 18–50% of the O_2 depletion could be attributed to warming over the 21st century (Bopp et al., 2013). It is also consistent with detailed analysis of observations for the relatively well observed North Atlantic for the past 50 years (Stendardo & Gruber, 2012), whereas the global analyses by Schmidtko et al. (2017) suggest a smaller value, albeit based on relatively sparse in situ observations.

During phase III, the simulated global ocean O_2 content fully recovers and even overshoots initial conditions with a 2.9 Pmol (1.3%) larger O_2 inventory by the end of the 4,500 year long simulation. The actual O_2 increase may even be larger, as the preindustrial control run simulates a deep ocean O_2 drift amounting −5.2 Pmol by Year 1500 (black dashed line in Figure 2a). The decrease in the O_2 inventory in the control simulation has been attributed to a long-term warming drift, lack of ventilation of the oldest waters leading to expansion of the suboxic zones, and the lack of representation of bubble injection processes during gas exchange. The inflection in the simulated global ocean O_2 content is unexpected since the global ocean
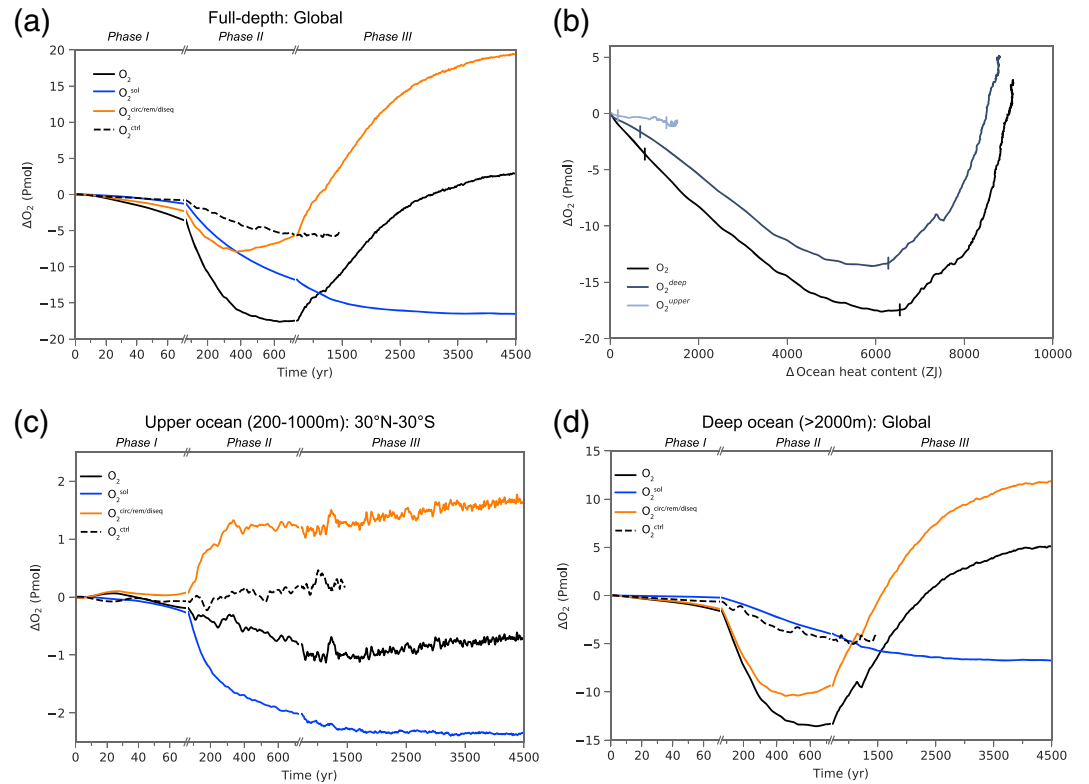
Figure 2. Simulated multimillennial changes in ocean O_2 inventory for the (a) full-depth global ocean, (c) averaged between 200 and 1,000 m and 30°S and 30°N, and (d) averaged below 2,000 m. (b) The relationship between global ocean, upper ocean (200–1,000 m) and deep ocean (below 2,000 m) heat content changes and O_2 inventory changes. The vertical bars in (b) denote the different phases.

temperature (red line in Figure 1b) and heat content (Figure 2b) continue to increase resulting in a continuing decrease in O_2^{sol} amounting to −16.0 Pmol by the end of the simulation (blue line in Figure 2a). In light of the transient simulation results for the 21st century (Bopp et al., 2013), one might expect this continued warming to lead to further deoxygenation. However, the large increase in $O_2^{circ/rem/diseq}$ (18.9 Pmol by the end of the simulation; orange line in Figure 2a) more than compensates the solubility-driven O_2 loss, thereby causing an overall increase in the global ocean O_2 inventory. The change in the oceanic O_2 content is linearly scaled to ocean heat content change during phase I, with a slope of −0.45 Pmol/10^{23}J ($R^2 > 0.99$), and phase II with a slope of −0.23 Pmol/10^{23}J ($R^2 = 0.94$). During phase III, both O_2 and heat content increase, with a slope of 0.94 Pmol/10^{23}J ($R^2 = 0.89$).

The simulated decrease and subsequent increase in the global oceanic O_2 inventory is associated with contrasting O_2 responses between the upper (sub)tropical oceans including the OMZs (200 to 1,000 m) and the
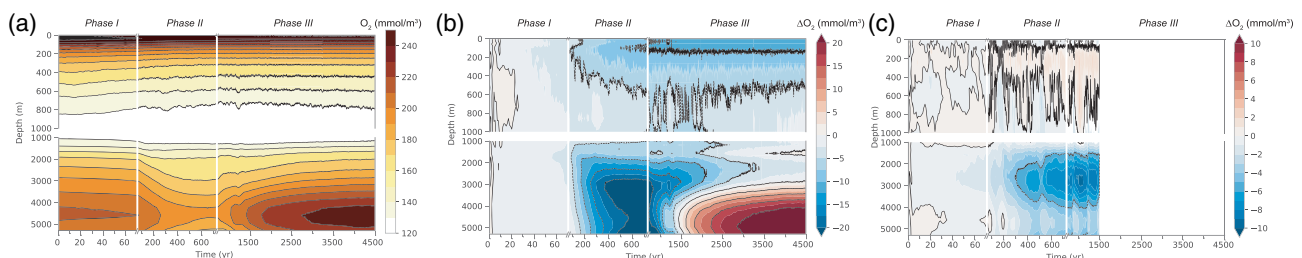

Figure 3. (a) Hovmöller diagram of simulated globally averaged O_2 concentration. (b) Same as (a) but shown as anomalies relative to Years 1–5. (c) Same as (b) but shown for the 1,500 year long preindustrial control simulation. Contour lines highlight the pattern structures.
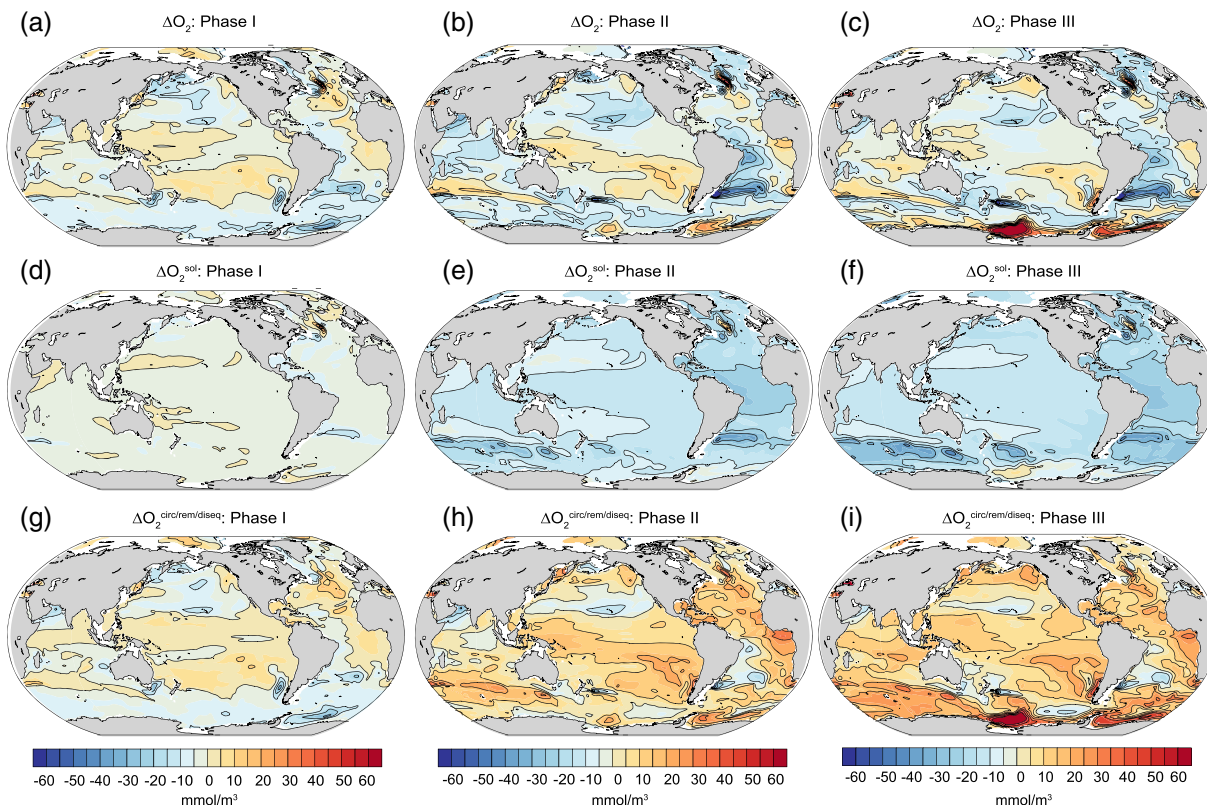
Figure 4. Simulated upper ocean (200–1,000 m) changes in (a–c) O_2, (d–f) O_2^{sol}, and (g–i) $O_2^{circ/rem/diseq}$ averaged over (a, d, and g) Years 61–80, (b, e, and h) Years 701–720, and (c, f, and i) Years 4481–4500 relative to the first 5 years of the simulation. Changes are shown as averages over 200–1,000 m. The black contours highlight pattern structures.

deep ocean (below 2,000 m; Figure 3). The upper ocean in the (sub)tropics experiences a small decrease in O_2 of about 5–10 mmol m^{-3} by the end of the simulation (Figure 3), whereas the deep ocean O_2 concentration content initially decreases by up to 30 mmol m^{-3} and then recovers and overshoots preindustrial values by more than 20 mmol m^{-3}. The processes leading to this contrasting O_2 response in the upper and deep ocean are discussed next.

3.2. Upper Ocean Deoxygenation in the Tropics

In the (sub)tropical upper (30°N–30°S, 200–1,000 m) ocean, where O_2 is generally low, the O_2 content decreases by 0.8 Pmol during the first two phases, that is, up to 720 years into simulation. It recovers only marginally during phase III (black line in Figure 2c), such that at the end of the simulation, the O_2 content is still 0.7 Pmol lower than at the beginning. As is the case for the global ocean O_2 content, most (77%) of the total O_2 decrease occurs during phase II, when atmospheric CO_2 has already stabilized. During phases I and II, the decrease in O_2^{sol} (blue line in Figure 2c) dominates the decrease in O_2. $O_2^{circ/rem/diseq}$ increases (orange line in Figure 2c), but the increase is smaller in magnitude than the decrease in O_2^{sol}. During phase III, the simulated increase in $O_2^{circ/rem/diseq}$ leads to a marginal recovery in O_2, as O_2^{sol} levels out during phase III.

The simulated spatial pattern of O_2 changes in the upper ocean (200–1,000 m) is rather heterogeneous (Figures 4a–4c). By the end of phase III, O_2 has decreased in the North and South Atlantic by up to 30 mmol m^{-3}. There are also regions, such as parts of the North Pacific and Southern Ocean, where O_2 has increased by the end of the simulation. The pattern of O_2 changes after phase II strongly resembles the pattern after phase III underscoring that the largest changes in the upper ocean occur during phase I and especially phase II. There are some exceptions, however. O_2 decreases during phases I and II and then
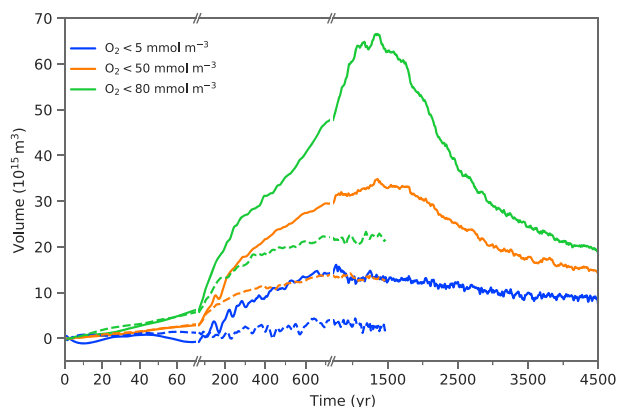
Figure 5. Simulated changes in the volume of oxygen minimum zones defined by O_2 thresholds of 5, 50, and 80 mmol m^{-3}, relative to the first 5 years of the simulation. Dashed lines denote the preindustrial control run.

increases strongly during phase III around Antarctica (see section 3.3) and also, yet to a lesser extent, in the Indian Ocean.

In the midlatitudes of the South Pacific, the increase in $O_2^{circ/rem/diseq}$ is larger than the decrease in O_2^{sol} leading to the overall increase in O_2 (Figure 4). This is not the case in the tropical Atlantic, where changes in O_2^{sol} are larger than changes in $O_2^{circ/rem/diseq}$, and therefore, O_2 decreases. In general, changes in $O_2^{circ/rem/diseq}$ largely explain the pattern of the O_2 changes.

The changes in the volume of the OMZs (Figure 5) mirror to some extent the changes in the upper ocean O_2 concentrations described above, irrespective of whether these regions are defined by a threshold of 50 or 80 mmol m^{-3}. OMZs expand substantially during phase I and especially during phase II. The near-anoxic regions ($O_2 < 5$ mmol m^{-3}) nearly double in volume ($+16 \cdot 10^{15}$ m^3 or $+44\%$). During phase III, the OMZs start to shrink but remain larger by the end of the simulation compared to preindustrial. Note that the volume of the OMZs increases over the course of the preindustrial control simulation (dashed lines in Figure 5), but this increase alone cannot explain the overall expansion of the OMZs in the 4,500 year-long simulation.

3.3. Deep Ocean Deoxygenation and Reoxygenation

In the deep ocean below 2,000 m (black line in Figure 2d), the dissolved O_2 inventory evolves fundamentally differently. The O_2 inventory decreases by 13 Pmol during phases I and II. However, the deep O_2 content recovers during phase III and overshoots preindustrial levels by the end of the simulation ($+5$ Pmol O_2) indicating that the recovery and overshoot of the global O_2 inventory (black line in Figure 2a) is largely driven by the increase in deep ocean O_2 content.

During phase I, deep ocean O_2 decreases by up to 20 mmol m^{-3} in the Weddell Sea and in the subtropical North Atlantic, whereas O_2 increases in the deep Indian Ocean (Figure 6a). During phase II, the North Atlantic O_2 content continues to decrease and particularly the deep equatorial and North Pacific in particular experience large O_2 declines (by up to -50 mmol m^{-3}; Figure 6b). In contrast, the O_2 content in the Weddell Sea, and more generally around the Antarctic continent and the Arabian Sea increases by up to 20 mmol m^{-3} by the end of phase II. Most of the trends reverse in phase III (Figure 6c). The deep ocean O_2 content increases almost everywhere, except in the north and equatorial Atlantic, the eastern tropical Pacific, and the Coral Sea. The strongest increases (by up to $+50$ mmol m^{-3}) occur in the Ross Sea and along the Antarctic continental and Chilean margins and to a lesser degree in the North Pacific.

The simulated global (Figure 2d) and regional (Figures 6a–6c) changes in deep ocean O_2 are predominantly driven by changes in $O_2^{circ/rem/diseq}$ (Figures 2d and 6g–6i) during all three phases. During phase II, $O_2^{circ/rem/diseq}$ increases in the Arabian Sea and the Southern Ocean, especially in the Weddell Sea, and this trend persists during phase III (Figures 6h and 6i). During phase III, $O_2^{circ/rem/diseq}$ also strongly increases in the Ross Sea, along the Chilean Margin and the North Pacific, in part opposite to the changes simulated during phase II. The large O_2 decrease in the equatorial Pacific during phase II is also mainly driven by a decrease in $O_2^{circ/rem/diseq}$. The simulated regional changes in O_2^{sol} are generally negative (Figures 6d–6f), yet more uniform and subdued than the changes in $O_2^{circ/rem/diseq}$.

3.4. Processes Controlling Changes in $O_2^{circ/rem/diseq}$

As discussed above, the spatial distribution of the O_2 changes in both the upper and deep ocean can mainly be explained by changes in $O_2^{circ/rem/diseq}$. The changes in O_2 driven by changes in O_2^{sol} are generally smaller, although still important, especially in the upper ocean. To explain the changes in $O_2^{circ/rem/diseq}$, we analyze the physical and biological factors controlling $O_2^{circ/rem/diseq}$, that is, changes in ventilation age (i.e., ideal age; Figure 7a) and net primary and export production (Figure 7b). We first discuss the changes in the upper ocean of the (sub)tropics and then in the deep ocean.

The increase in $O_2^{circ/rem/diseq}$ in the upper ocean of the (sub)tropics during phase I and in the early part of phase II is associated with a large decrease (-70 years) in ventilation age—the average time required for
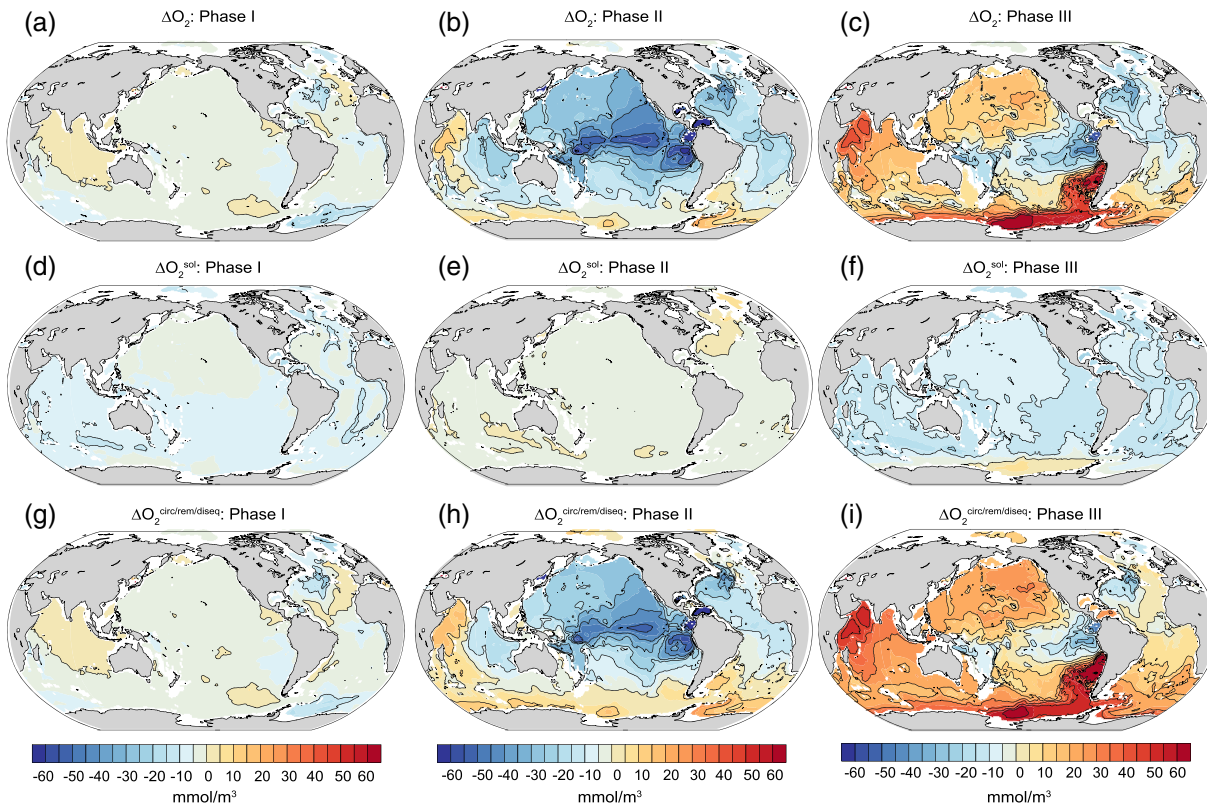
Figure 6. Simulated deep ocean changes in (a–c) O_2, (d–f) O_2^{sol}, and (g–i) $O_2^{circ/rem/diseq}$ in (a, d, and g) Years 61–80, (b, e, and h) Years 701–720, and (c, f, and i) Years 4481–4500 relative to the first 5 years of the simulation. Changes are shown as averages between 2,000 m and the bottom of the ocean. The black contours highlight pattern structures.

waters to travel from the surface to 200–1,000 m depth interval (orange line in Figure 7a), particularly in the equatorial Pacific (Figures 8a and 8b). Concurrently, net primary production (blue dashed line in Figure 7b), export production (orange dashed line in Figure 7b) and by inference the respiratory O_2 demand in the upper ocean decrease during phase I (Figure 8g and 8h). Thus, both increased ventilation and the reduced O_2 consumption from remineralization contribute to the increase in $O_2^{circ/rem/diseq}$. The latter process might be even underestimated in our model, since compared to other CMIP5-type Earth system models, its simulated reduction in NPP and export production in response to transient global warming tend to be on the low end of the range (Laufkötter et al., 2015, 2016).
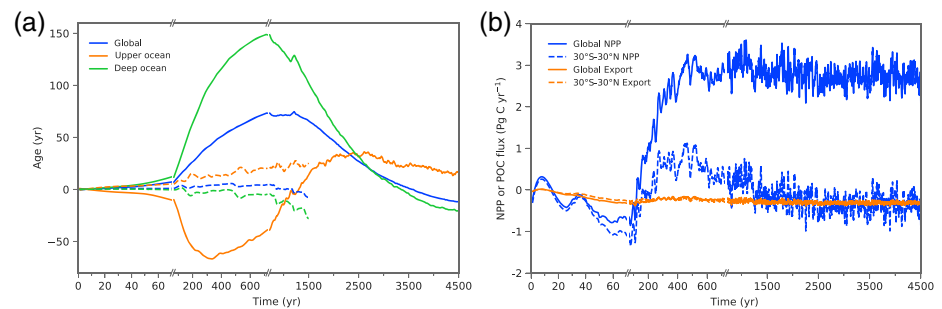

Figure 7. Simulated changes in (a) the ideal age for the global ocean (blue line), the upper 200–1,000 m ocean between 30°S and 30°N (orange) and the global deep ocean below 2,000 m (green), as well as (b) the export production (i.e., particulate organic carbon flux at 100 m depth; blue line) and net primary production integrated over the top 100 m of the ocean (NPP; orange) for the global ocean (solid lines) and averaged between 30 S and 30°N (dashed lines). Dashed lines in (a) indicate the results from the preindustrial control simulation. The time series have been smoothed with a Savitzky-Golay filter with a window size of 51 years.
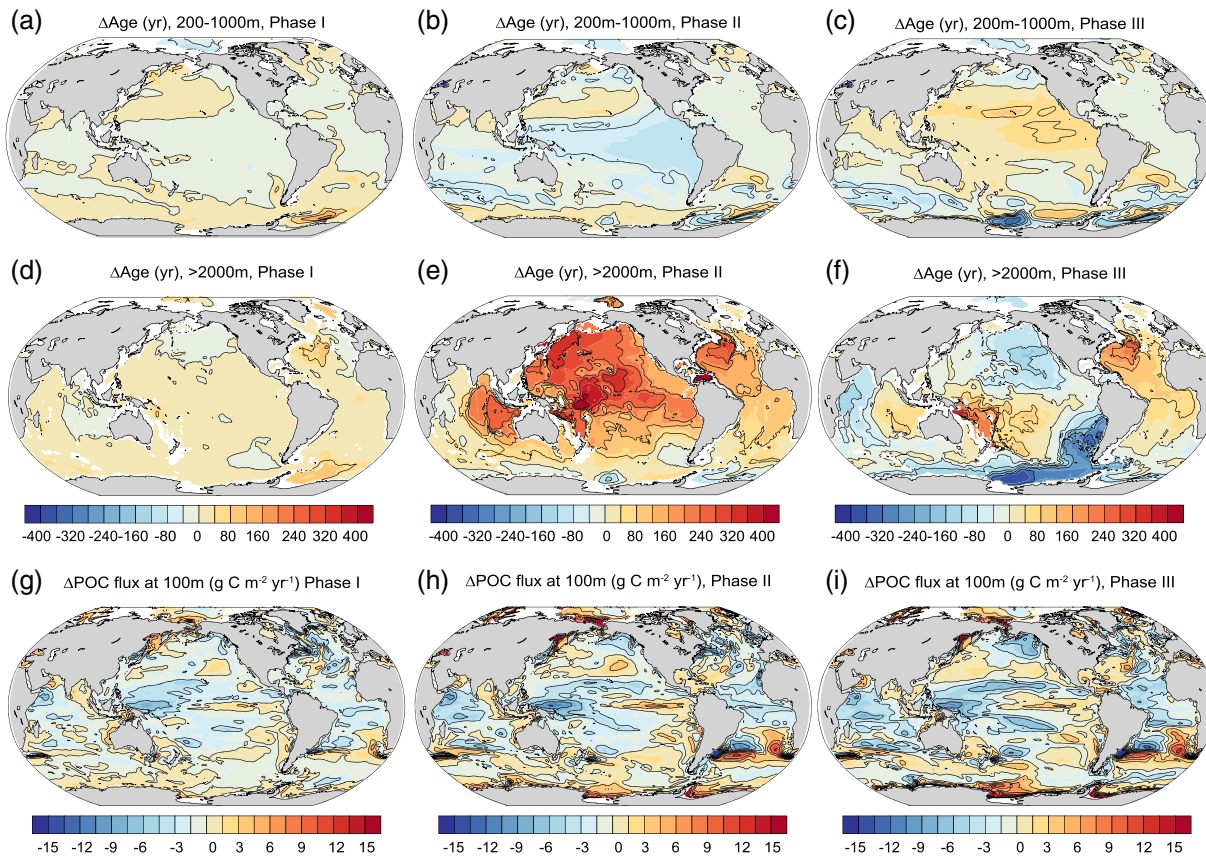
Figure 8. Simulated changes in ideal age for the (a–c) upper 200–1,000 m and for the (d–f) deep ocean for all three phases. (g–i) Simulated changes in export production of particulate organic carbon (POC) at 100 m depth. All changes are shown relative to the first 5 years of the simulation. The black contours in all panels highlight the pattern structures.

After about 450 years, ventilation ages in the upper ocean of the (sub)tropics increase again and overshoot the preindustrial water mass age by Year 2500 (Figure 7a). Afterward, ventilation ages decrease slowly but remain higher than under preindustrial conditions. In particular, the upper waters of the tropical and mid-latitude Pacific Ocean are bathed by older waters by the end of the simulation (Figure 8c). During phases II and III, export production in the (sub)tropics continues to decrease slightly (Figure 7b), leading to total reduction of −4% or −0.3 Pg C/year integrated by the end of phase III. Interestingly, this decrease in export production occurs while NPP in the sub (tropics) temporarily increases by 2% or 0.8 Pg C/year during phase II (blue dashed line in Figure 7b). This decoupling between export production and NPP could be a consequence of the strong temperature dependence of the phytoplankton growth rates responding to the higher temperatures and a decreasing export efficiency due to a shift in the phytoplankton production toward small phytoplankton (Laufkötter et al., 2016).

Next, we turn our discussion to drivers of $O_2^{circ/rem/diseq}$ changes in the deep ocean. The regional changes in ventilation time during all three phases (Figures 8d–8f) strongly correlate with changes in deep ocean $O_2^{circ/rem/diseq}$ (Figures 4g–4i). The ventilation age strongly decreases in the Southern Ocean and in the Ross Sea, as well as in the Arabian Sea and along the Chilean Margin during phase III (Figure 8f). The North Pacific becomes first more sluggishly ventilated during phase II (Figure 8e) leading to a decrease in $O_2^{circ/rem/diseq}$ (Figure 6), but then during phase III, it becomes better ventilated (Figure 8f) and oxygenated (Figure 6i). In contrast, the deep North Atlantic remains less ventilated until the end of the simulation. The simulated overall decrease in export production (orange solid line in Figure 7b) and associated reduction in O_2 consumption may also contribute to the O_2 increase in the abyssal ocean. However, the strong correlation between changes in ventilation age and O_2 changes indicate that changes in export production are not the main drivers of deep ocean O_2 changes. An exception relates to the eastern equatorial Pacific, where O_2 decreases
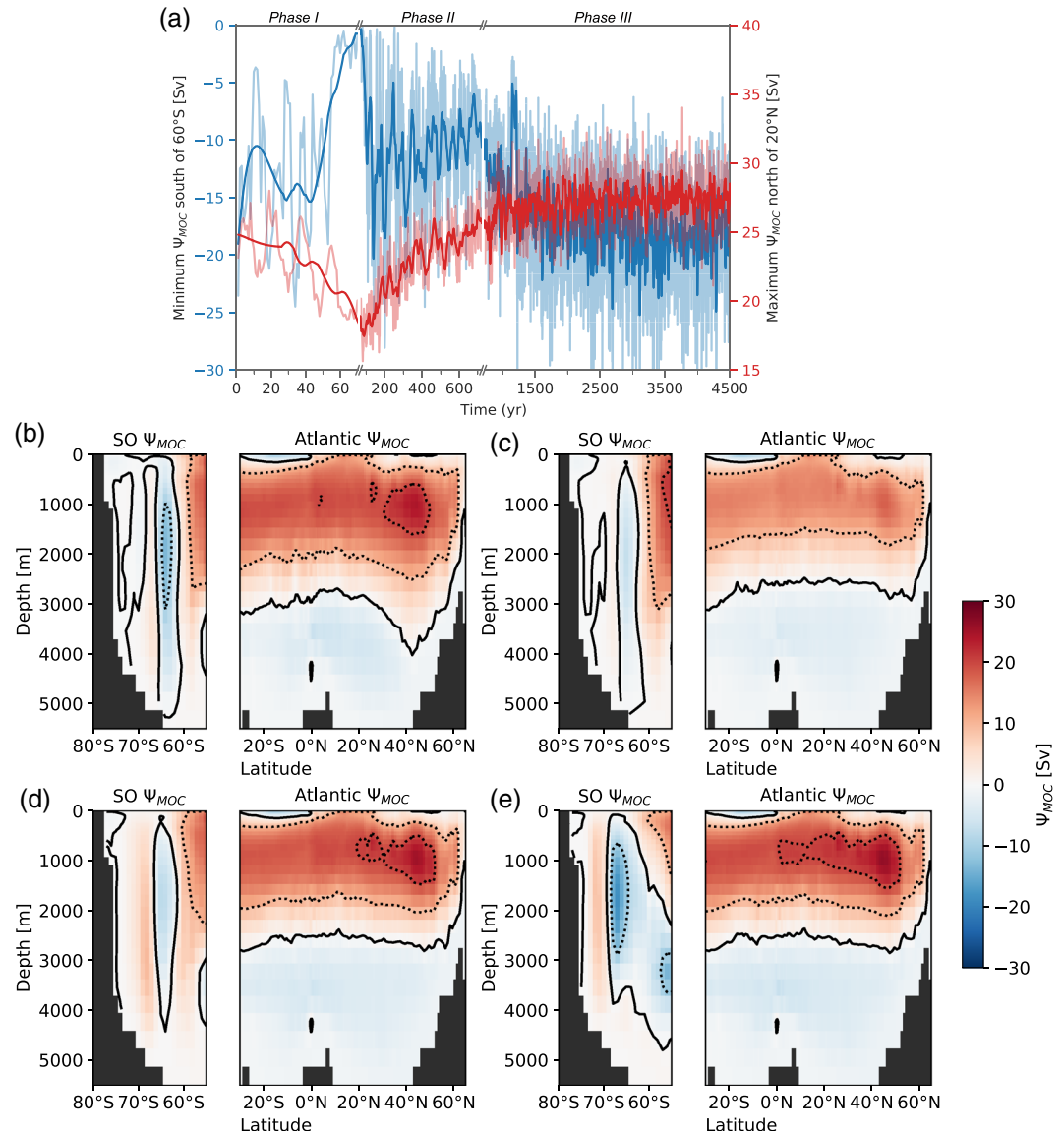
Figure 9. (a) Time series of the minimal global meridional overturning circulation (MOC) south of 60°S (blue, left y axis) and maximal Atlantic MOC north of 20°N (red, right y axis). Note that more negative SMOC values correspond to a stronger SMOC. The transparent and full lines show the annual and smoothed data using a Savotzky-Golay filter with a window size of 51 years, respectively. (b–e) Latitude-depth plots of the mean Southern Ocean (SO, left panels) and Atlantic (right panels) meridional overturning stream function (ψ_{MOC}) for the (b) first 5 years of the simulation and the last 20 years of phases (c) I, (d) II, and (e) III.

(Figure 6c) even though ventilation age changes remain small (Figure 8f). The O_2 decreases there may be explained by an increase in export production (Figure 8i) and deep O_2 consumption due to the vertical expansion of the OMZs above that reduces O_2 consumption in the upper ocean.

3.5. Long-Term Recovery of the Southern Ocean Ventilation

Next, we consider the processes leading to the ventilation increase in the Southern Ocean at the onset of phase III. The AMOC decreases from 25.0 Sv (1 Sv = 10^6 m^3 s^{-1}) to 15.6 Sv during the first 80 years of the simulation but then recovers and overshoots its initial value after 1,000 years by nearly 10% (red line in Figure 9a). The AMOC decrease and "overshoot" is qualitatively in line with previous coupled climate model simulations (e.g., Battaglia & Joos, 2018; Krasting et al., 2018; Rugenstein et al., 2016; Schmittner et al., 2008; Zickfeld et al., 2013). The AMOC becomes shallower during phase I and remains relatively shallow even
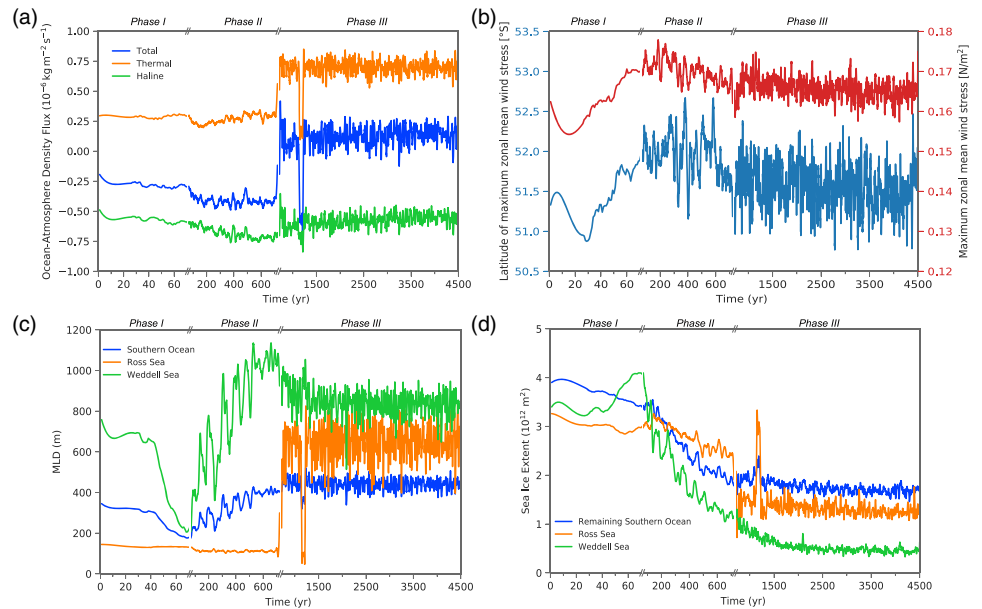
Figure 10. (a) Simulated changes in total, thermal, and haline surface density flux in the Ross Sea. The total surface density flux (F_ρ) is the sum of the thermal ($F_{\rho,thermal}$) and haline ($F_{\rho,haline}$) density fluxes. (b) Simulated changes in latitude and intensity of maximum zonal mean wind stress over the Southern Ocean. (c and d) Simulated changes in (c) September mean mixed layer depth (MLD) and (d) annual sea ice extent. The Southern Ocean is defined as the region south of 55°S, the Ross Sea south of 55°S and between 170°E and 120°W, the Weddell Sea south of 55°S between 70°W and 30°E, and the remaining Southern Ocean is defined as the region south of 55°S without the Ross Sea and Weddell Sea regions. All time series have been smoothed with a Savitzky-Golay filter with a window size of 51 years.

after its reinvigoration (Figures 9b–9e). This may explain the increase in ventilation age (Figure 8f) and the decrease in O_2 (Figure 6c) in the deep North Atlantic by the end of phase III.

Similarly, the SMOC reaches its weakest state (−0.2 Sv) soon after atmospheric CO_2 has stabilized (blue line in Figure 9a). In contrast to the AMOC, the SMOC does not steadily converge to a new equilibrium thereafter. Within the first few decades after the minimum strength, SMOC recovers to its preindustrial strength but then weakens again until the end of phase II. However, the small weakening is superimposed by large interannual variability. At the beginning of phase III, the SMOC increases again and reaches a new equilibrium strength of −18.5 Sv by the end of phase III (38% stronger than at preindustrial). This strengthening leads to a stronger ventilation of the deep Southern Ocean and subsequently parts of the Indo-Pacific Ocean (Figure 8f) and, therefore, to an increase in $O_2^{circ/rem/diseq}$ (Figure 6i) and O_2 levels (Figure 6c).

The abrupt reinvigoration of the SMOC is somewhat unexpected, as the thermal and especially the haline surface density flux actually decrease during phases I and II (Figure 10a)—circumstances that are expected to lead to enhanced water-column stratification and a reduction of the formation of Antarctic Bottom Water (de Lavergne et al., 2014). Changes in atmospheric wind patterns over the Southern Ocean also cannot explain the sudden onset of deepwater formation in the Southern Ocean. During phase I, the model simulates a poleward shift of the Southern Hemisphere westerlies by about 1° (blue line in Figure 10b) and a small strengthening (red line in Figure 10b). Both changes are common features simulated in Earth system models under transient global warming (Russell et al., 2006). However, during phases II and III, the westerlies gradually weaken and move equatorward. Thus, they do not show any sudden changes in intensity or position that could explain the abrupt onset of deepwater formation.

The abrupt increase in SMOC during the transition from phases II to III is primarily driven by the onset of deepwater formation in the Ross Sea. The September mixed layer in the Ross Sea abruptly deepens from about 170 m to more than 600 m within a few years (orange line in Figure 10c) with a concomitant abrupt sea ice retreat (orange line in Figures 10d and 11). In contrast, the mixed layer in the Weddell Sea steadily deepens during phase II after an initial shoaling (green line in Figures 10c and 10d). Also, the sea ice extent in the Weddell Sea changes only gradually. Thus, the changes in the Weddell Sea cannot be responsible for
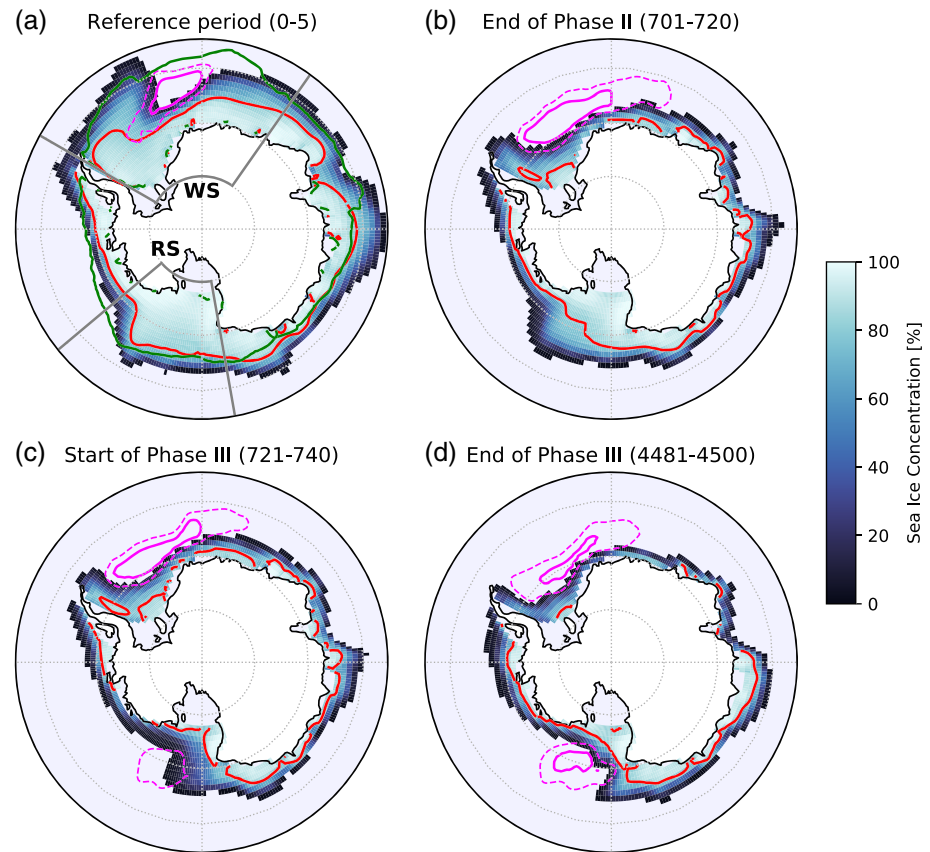
Figure 11. September sea ice concentration in the Southern Ocean for the (a) first 5 years of the simulation, (b) end of phase II (average over period 701 to 720), (c) start of phase III (average over period 721 to 740), and (d) end of phase III (average over period 4481–4500). The simulated 80% sea ice concentration contour is shown in red, and the September mixed layer depth contours of 2,000 and 4,000 m are shown as magenta dashed and solid lines, respectively. In (a), the green line shows the observation-based 80% sea ice concentration contour averaged over the 1986–2005 period (Rayner et al., 2003) and the gray solid lines depict the boundaries of the Ross Sea (RS) and Weddell Sea (WS) region, respectively.

the abrupt increase in SMOC. But the Weddell Sea is likely responsible for the partial SMOC recovery at the beginning of phase II and the partial recovery and the slowdown in $O_2^{circ/rem/diseq}$ decrease toward the end of phase II (Figure 2d).

Which processes lead to the abrupt change in the mixed layer depth in the Ross Sea? During phases I and II, the uppermost 75 m of the Ross Sea waters freshen (decrease in salinity; Figure 12b) due to an increase in precipitation and in melting rates (green line in Figure 10a). This freshening together with a very small warming (Figure 12) decreases surface density (Figure 12d) and increases the vertical stratification of the upper water column as expressed by the squared Brunt-Väisälä frequency (Figure 12c). This increase in the stratification reduces the transport and mixing of subsurface waters, which usually carry saltier and warmer waters toward the surface, where they are cooled by the atmosphere and freshened by an excess of freshwater input from the atmosphere and the melting of sea ice (Haumann et al., 2020). Through the reduction in this upward transport and mixing, the increased stratification leads to a buildup of positive anomalies in temperature (up to 1.5°C; Figure 12a) and in salinity (up to 0.1 psu; Figure 12b) below ~75 m. These anomalies tend to compensate each other in terms of their effect on subsurface density (Figures 12d–12f). However, as outlined by Martin et al. (2013), these subsurface changes prime the system toward a potential instability. This can happen once these anomalies breach the stratification and make it to the surface. There the warm waters would lose their signal quickly through cooling by the atmosphere, while the excess salinity would stay behind, as the freshening occurs more slowly. This leads then to especially dense surface waters which can rapidly initiate deep convection. In addition to this priming effect by the accumulation of heat and excess
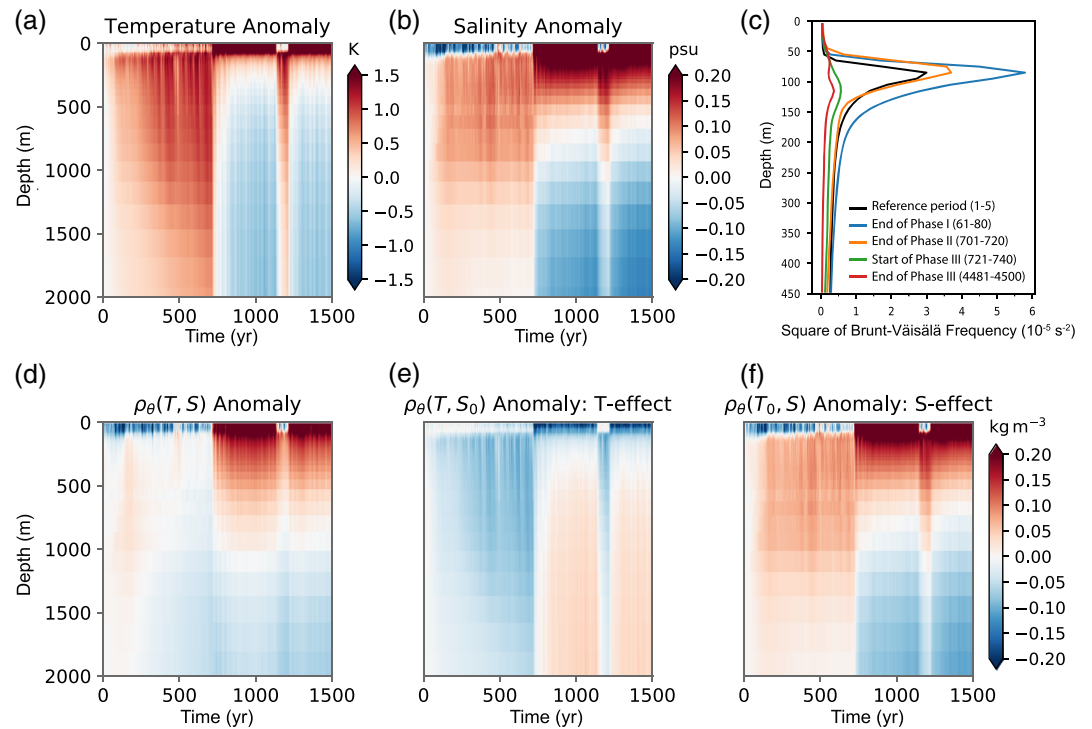
Figure 12. Depth-time Hovmöller diagrams of simulated annual mean anomalies in the Ross Sea of (a) temperature, (b) salinity, (d) potential density, (e) potential density based on preindustrial period salinity, and (f) potential density based on preindustrial period temperature. (c) Vertical upper ocean profiles of the squared Brunt-Väisälä averaged over different periods of the simulation. The Ross Sea is defined as the region south of 55°S and between 170°E and 120°W.

salinity at depth, sea ice is continually retreating during phases I and II (Figures 11a and 11b) permitting a rapid cooling through heat release into the atmosphere when these warm and salty water mass eventually reach the surface. Therefore, at the end of phase II, the Ross Sea is optimally primed by meeting several conditions that favor open ocean deep convection.

During the transition from phases II to III, the deep water formation initiates in the Ross Sea, which results in an abrupt change in density, temperature, and salinity structure within only a few years (Figure 12) as well as to intensified sea ice melting (orange line in Figures 10d and 11c) and enhanced air-sea heat flux (orange line in Figure 10a). The onset of deepwater formation also leads to a rapid increase in atmospheric temperature south of 55°S (orange line in Figure 1b). The open ocean deep convection in the Ross Sea persists throughout phase III, with the exception of the 1150–1200 period. In the new equilibrium, the water column is well mixed in the upper 500 m (Figure 12c). The exact timing of the abrupt increase in deep water formation in the Ross Sea is stochastic in nature, in agreement with previous modeling studies (Martin et al., 2013). We demonstrate this by using an additional simulation that was run over the period 673–822 with identical forcing but started from slightly different initial conditions (see section 2.2 for description of the simulation). The onset of the deepwater formation in the Ross Sea is shifted by 22 years between the two simulations (not shown) pointing to the stochastic nature of the deepwater formation onset. However, certain preconditioning such as high subsurface salinity must be met so that deep water formation can occur.

4. Discussion and Conclusion

Our study suggests that a millennial-scale recovery and strengthening of the deep Southern Ocean ventilation leads to a global ocean reoxygenation under long-term global warming. Even though the substantial warming of the whole ocean (1.7°C) drives the global O_2 content down (O_2^{sol}), the increase in O_2 driven by enhanced ventilation and by a reduced O_2 demand from the biological pump ($O_2^{circ/rem/diseq}$)

overcompensates this solubility-driven reduction. This long-term equilibrium response to global warming is opposite to that occurring during the transient warming on centennial timescales, when both circulation and solubility tend to reinforce each other. This difference between the transient and the long-term equilibrium response of O_2 to global warming is largely driven by the deep ocean, reflecting its dominating contribution to the O_2 inventory of the ocean. Oxygen in the upper ocean of the low latitudes and especially in the OMZ responds in a distinctly different manner. There, O_2 decreases on centennial timescales and remains depressed on millennial timescales. This is a consequence of the effect of warming never being compensated by ventilation/biology on all timescales.

Our result of a continued loss of O_2 in the (sub)tropical upper ocean and an associated expansion of OMZs under protracted global warming appears to be in contrast to the results from Fu et al. (2018). Using simulations with the NCAR CESM1 up to the Year 2300 under the RCP8.5 scenario and its extension, they show that after nearly two centuries of declining O_2 trends, the O_2 content of the tropical upper ocean undergoes a strong trend reversal around 2150, resulting in a near-full recovery of the O_2 concentration and the OMZ volume back to the preindustrial state. Unfortunately, the results from the two studies cannot be compared directly, since the two simulations employed two very different forcing scenarios, that is, 1% increase in atmospheric CO_2 for 70 years up to nearly 600 ppm, followed by a fixed forcing in our case, versus a slower increase over 400 years all the way up to about 2,000 ppm in the Fu et al. case. The achieved global ocean warming in the latter simulation was nearly 6°C, while it is less than 2°C in our simulation. In addition, the two studies compared two rather different time periods, that is, 200 years during which the forcing continued to increase, versus a multicentury to millennial response after the forcing had been stabilized in our case. Still, the two very different responses to ocean warming hold two important messages.

First, it points to the fundamental challenge associated with the modeling of the O_2 content of the tropical upper ocean (cf. Cabré et al., 2015; Cocco et al., 2013). Changes in the O_2 concentration in these regions are often the net result of strongly opposing tendencies stemming from warming/solubility and circulation/biology, with subtle changes in either of the two leading to fundamentally different net results. Similar to our study, Fu et al. (2018) also find that the export production decreases and that the ventilation slightly increases, overcompensating the solubility-driven loss of O_2. In our simulation, however, the ventilation decreases toward the end of the simulation and the solubility-driven decrease in O_2 overcompensates any O_2 change due to the decrease in biological production and the changes in ventilation. The global export production decreases only by a few percent in the GFDL-ESM2M (Figure 7b), whereas the global export production declined by about 30% in the model simulations analyzed in the Fu et al. study (Moore et al., 2018).

The second message emerging from the comparison is that both studies emphasize that when it comes to O_2 changes in the tropical upper ocean under global warming, trends during one phase of a transient (e.g., 21st century) cannot be extrapolated to another phase of the transient (22nd century). And even further, trends during any phase of a transient cannot be used as an indication for what the final equilibrium response to warming will be. We conclude that there is high uncertainty in how the ocean and its biogeochemistry will change under long-term global warming. So far, the climate modeling community has strongly focused on centennial timescales and developed the model components needed for that relatively short timescale. However, to understand the millennial-scale equilibrium response of the Earth system to global warming, we need to focus on the processes that impact the Earth system on these long timescales, such as ice sheet-ocean interactions, and the representation of the deepwater formation and the biological pump.

Our simulation indicates a strong recovery of the deep ocean ventilation under a warming climate. Similar deep ocean circulation changes have been simulated in previous multicentennial to millennial global warming simulations with reduced-complexity models (Battaglia & Joos, 2018; Bi et al., 2001; Ridgwell & Schmidt, 2010; Rugenstein et al., 2016; Schmittner et al., 2008). Using different greenhouse gas scenarios, these studies show a decrease in the Antarctic Bottom Water formation with transient global warming but a partial or full recovery under a (nearly) equilibrated warmer climate. The only available study to date using a comprehensive ESM to investigate changes in deep ocean ventilation and oxygenation on millennial timescales confirms our findings (Yamamoto et al., 2015). They also show that the SMOC recovers after approximately 500 to 700 years followed by a subsequent oxygenation of the deep ocean. However, Yamamoto et al. (2015) suggest that the recovery of the deep ocean ventilation is entirely caused by the recovery of the Weddell Sea convection, in contrast to our simulation suggesting strong Ross Sea convection under

warming climate in addition to Weddell Sea convection. Yamamoto et al. (2015) also suggests that the O_2 decrease in the deep North Atlantic may be caused by a weaker AMOC. However, in our simulation, the AMOC recovers, but O_2 remains low. The reduced ventilation and associated O_2 decrease is rather caused by the shallowing of the AMOC cell, which leads to less ventilation of the deep North Atlantic even under a stronger AMOC. As neither Yamamoto's ocean model nor our model includes an interactive ice sheet and both models have a relatively coarse resolution, the results of both studies should be viewed with caution.

Our results of a better ventilated and oxygenated deep ocean but a less oxygenated upper ocean under a warming climate is also consistent with marine proxy records that indicate generally lower O_2 levels in the deep ocean yet higher O_2 concentrations in the upper ocean during the last glacial period (Galbraith & Jaccard, 2015; Jaccard et al., 2014; Jaccard & Galbraith, 2012). Interestingly, the deep ocean became better oxygenated as the Earth climate emerged from the last ice age as deep ocean ventilation increased in the Southern Ocean, possibly associated with sea-ice retreat and/or wind shifts (Jaccard et al., 2016; Skinner et al., 2010). In any case, additional long-term simulations with Earth system models are needed to systematically assess changes in the ocean beyond 2100.

Our simulation suggests that in both, the upper and deep ocean, the largest changes in O_2 occur many centuries or even millennia after atmospheric CO_2 has stabilized. In fact, about 80% of the deep ocean and subsurface ocean O_2 decrease occurs after atmospheric CO_2 has stabilized. Therefore, the largest impacts on marine life may occur long after the stabilization of the radiative forcing. In the geological past, reductions in intermediate-water O_2 had significant impacts on marine biodiversity and functioning (Moffitt et al., 2015; Myhre et al., 2017). In the upper ocean at low latitudes, where O_2 levels are already low, a decrease in O_2 may have a wide range of biological, ecological, and biogeochemical consequences, including shifts in body size, taxonomic composition, diversity, lifestyles, life stage, and trophic patterns of marine organisms (Breitburg et al., 2018; Cheung et al., 2013; Levin, 2018) as well as changes in ocean biogeochemistry, primarily the marine nitrogen cycle with consequences for marine productivity (Gruber, 2008). A large decrease in O_2 may therefore have deleterious consequences on marine life, in addition to stress arising from other adverse ocean ecosystem drivers such as heatwaves, acidification, and nutrient stress (Bopp et al., 2013; Frölicher et al., 2016, 2018; Gruber, 2011).

Even though our simulated O_2 changes, in particular the deep ocean O_2 changes, compare qualitatively well with the past O_2 changes covering the last deglaciation and with recent simplified ESM simulations, a number of caveats need to be discussed. First and most importantly, the model lacks a dynamic ice sheet component, and meltwater input (and albedo changes) from Antarctic and Greenland ice melting is not included. Any additional freshwater might lead to a larger reduction in the SMOC and AMOC than simulated in our study and might strongly delay or prohibit the recovery of the SMOC and AMOC and consequently also deep ocean O_2. However, the mechanism (surface freshening and subsurface warming) responsible for the SMOC recovery seen in our simulation may also be at play under an even stronger stratification with stronger surface freshening but also stronger subsurface warming.

Second, the GFDL-ESM2M predominantly forms deep water in the Southern Ocean through open ocean convection in the Weddell Sea, illustrated by the overly deep mixed layer and low bias in sea ice extent in this region (Figure 11a). The combination of sea ice and iceberg export of freshwater and winter heat loss leads to open ocean convection in the Weddell Sea in the GFDL-ESM2M. In the "real" Southern Ocean, deep waters are predominantly formed on the continental shelves of the Weddell and Ross Sea through brine rejection and interactions with grounded ice sheets (Drucker et al., 2011; Orsi, 2010) and only rarely in open ocean polynyas (Killworth, 1983). Therefore, the resupply of O_2 to the deep ocean through Southern Ocean deep water formation in the Ross and Weddell Sea in the GFDL-ESM2M may not be realistic. However, no Earth system model currently represents the complex physical processes in the Southern Ocean correctly (Heuzé, 2020), because in part the resolution is too coarse, and in part the models are missing some crucial processes, such as cooling underneath the glacial ice.

Third, current ESMs including GFDL-ESM2M show large discrepancies in simulating present-day and future trends in OMZs and generally overestimate the observed OMZ volume (Cabré et al., 2015; Cocco et al., 2013; Fu et al., 2018). Higher resolution ESMs will hopefully improve the representation of OMZs

and deep water formation in the Southern Ocean and offer an improved way for investigating the response of OMZs and the Southern Ocean circulation to global warming (e.g., Busecke et al., 2019; Morrison et al., 2016; Newsom et al., 2016). However, the length of such high-resolution model simulations will be restricted to a few hundred years due to the enormous computational costs. To extend such high-resolution simulations to the millennial timescale will require a significant increase in community-level computational resources.

Fourth, the magnitude and timescale of response of the meridional overturning circulation is sensitive to the selected forcing scenario (Battaglia & Joos, 2018; Rugenstein et al., 2016; Stouffer & Manabe, 2003) and model formulation, and the SMOC as well as the AMOC may not recover under stronger greenhouse gas forcing scenarios. This limitation could be overcome by analyzing a suite of different multimillennial global warming simulations. The new LongRunMIP offers such a unique opportunity (Rugenstein et al., 2019).

And fifth, the TOPAZv2 lacks certain processes that may alter future O_2 changes in addition to the processes that we describe above. For example, recent studies have indicated that the carbon-to-nitrogen utilization ratio of organic matter production and therefore O_2 respiration may increase under higher ocean carbon conditions (Riebesell et al., 2007). While these perturbations to the nutrient cycling may alter the ocean's O_2 content (Oschlies et al., 2008), these changes would mainly be restricted to the upper ocean. In addition, the TOPAZv2 module does not include a temperature dependent remineralization (Bendtsen et al., 2015; Laufkötter et al., 2017) and particulate sinking speed, and therefore, a possible decreasing or increasing transfer efficiency of organic matter to the deep sea under global warming cannot be ruled out as an additional driver of upper and deep O_2 changes in the real world. Also, the potential changes in atmospheric nutrient deposition and sediment interactions are not considered here.

In summary, our study suggests that the equilibrium response in oceanic O_2 is not simply a scaled version of the transient response, especially in the deep ocean, and that future changes in O_2 may occur centuries after atmospheric CO_2 has stabilized. Given the potential for substantial long-term multimillennial-scale changes in ocean O_2 under a doubling of atmospheric CO_2, this study provides further evidence that future global warming should be kept at a minimum to prevent substantial and sustained negative impacts on marine life.

Data Availability Statement

Code and data can be found under: https://doi.org/10.5281/zenodo.3982620.

References

Anderson, J. L., Balaji, V., Broccoli, A. J., Cooke, W. F., Delworth, T. L., Dixon, K. W., et al. (2004). The new GFDL global atmosphere and land model AM2-LM2: Evaluation with prescribed SST simulations. *Journal of Climate*, *17*(24), 4641–4673. https://doi.org/10.1175/JCLI-3223.1

Battaglia, G., & Joos, F. (2018). Hazards of decreasing marine oxygen: The near-term and millennial-scale benefits of meeting the Paris climate targets. *Earth System Dynamics*, *9*(2), 797–816. https://doi.org/10.5194/esd-9-797-2018

Bendtsen, J., Hilligsøe, K. M., Hansen, J. L. S., & Richardson, K. (2015). Analysis of remineralisation, lability, temperature sensitivity and structural composition of organic matter from the upper ocean. *Progress in Oceanography*, *130*, 125–145. https://doi.org/10.1016/j.pocean.2014.10.009

Bi, D., Budd, W. F., Hirst, A. C., & Wu, X. (2001). Collapse and reorganisation of the Southern Ocean overturning under global warming in a coupled model. *Geophysical Research Letters*, *28*(20), 3927–3930. https://doi.org/10.1029/2001GL013705

Bianchi, D., Dunne, J. P., Sarmiento, J. L., & Galbraith, E. D. (2012). Data-based estimates of suboxia, denitrification, and N_2O production in the ocean and their sensitivities to dissolved O2. *Global Biogeochemical Cycles*, *26*, GB2009. https://doi.org/10.1029/2011GB004209

Bindoff, N. L., Cheung, W. W. L., Kairo, J. G., Arístegui, J., Guinder, V. A., Hallberg, R., et al. (2019). Changing ocean, marine ecosystems, and dependent communities. In H.-O. Pörtner et al. (Eds.), *IPCC Special Report on the Ocean and Cryosphere in a Changing Climate*. In Press

Bopp, L., Resplandy, L., Orr, J. C., Doney, S. C., Dunne, J. P., Gehlen, M., et al. (2013). Multiple stressors of ocean ecosystems in the 21st century: Projections with CMIP5 models. *Biogeosciences*, *10*(10), 6225–6245. https://doi.org/10.5194/bg-10-6225-2013

Bopp, L., Resplandy, L., Untersee, A., Le Mezo, P., & Kageyama, M. (2017). Ocean (de)oxygenation from the Last Glacial Maximum to the twenty-first century: Insights from Earth system models. *Philosophical Transactions of the Royal Society A - Mathematical Physical and Engineering Sciences*, *375*, 20160323. https://doi.org/10.1098/rsta.2016.0323

Breitburg, D., Levin, L. A., Oschlies, A., Grégoire, M., Chavez, F. P., Conley, D. J., et al. (2018). Declining oxygen in the global ocean and coastal waters. *Science*, *359*(6371), eaam7240. https://doi.org/10.1126/science.aam7240

Busecke, J. J. M., Resplandy, L., & Dunne, J. P. (2019). The equatorial undercurrent and the oxygen minimum zone in the Pacific. *Geophysical Research Letters*, *46*, 6716–6725. https://doi.org/10.1029/2019GL082692

Cabré, A., Marinov, I., Bernardello, R., & Bianchi, D. (2015). Oxygen minimum zones in the tropical Pacific across CMIP5 models: Mean state differences and climate change trends. *Biogeosciences*, *12*(18), 5429–5454. https://doi.org/10.5194/bg-12-5429-2015

Cheung, W. W. L., Sarmiento, J. L., Dunne, J., Frölicher, T. L., Lam, V. W. Y., Deng Palomares, M. L., et al. (2013). Shrinking of fishes exacerbates impacts of global ocean changes on marine ecosystems. *Nature Climate Change*, *3*(3), 254–258. https://doi.org/10.1038/nclimate1691

Cocco, V., Joos, F., Steinacher, M., Frölicher, T. L., Bopp, L., Dunne, J., et al. (2013). Oxygen and indicators of stress for marine life in multi-model global warming projections. *Biogeosciences*, *10*(3), 1849–1868. https://doi.org/10.5194/bg-10-1849-2013

Collins, M., Knutti, R., Arblaster, J., Dufresne, J.-L., Fichefet, T., Friedlingstein, P., et al. (2013). Long-term climate change: Projections, commitments and irreversibility. In T. F. Stocker et al. (Eds.), *Climate Change 2013 the Physical Science Basis: Working Group I Contribution to the Fifth Assessment Report of the Intergovernmental Panel on Climate Change* (pp. 1029–1136). Cambridge, United Kingdom and New York, NY, USA: Cambridge University Press.

de Lavergne, C., Palter, J. B., Galbraith, E. D., Bernardello, R., & Marinov, I. (2014). Cessation of deep convection in the open Southern Ocean under anthropogenic climate change. *Nature Climate Change*, *4*(4), 278–282. https://doi.org/10.1038/nclimate2132

Deutsch, C., Ferrel, A., Seibel, B., Pörtner, H.-O., & Huey, R. B. (2015). Climate change tightens a metabolic constraint on marine habitats. *Science*, *348*(6239), 1132–1135. https://doi.org/10.1126/science.aaa1605

Drucker, R., Martin, S., & Kwok, R. (2011). Sea ice production and export from coastal polynyas in the Weddell and Ross Seas. *Geophysical Research Letters*, *38*, 1991–2002. https://doi.org/10.1029/2011GL048668

Dunne, J. P., John, J. G., Adcroft, A. J., Griffies, S. M., Hallberg, R. W., Shevliakova, E., et al. (2012). GFDL's ESM2 global coupled climate-carbon earth system models. Part I: Physical formulation and baseline simulation characteristics. *Journal of Climate*, *25*(19), 6646–6665. https://doi.org/10.1175/JCLI-D-11-00560.1

Dunne, J. P., John, J. G., Shevliakova, E., Stouffer, R. J., Krasting, J. P., Malyshev, S. L., et al. (2013). GFDL's ESM2 global coupled climate-carbon earth system models. Part II: Carbon system formulation and baseline simulation characteristics. *Journal of Climate*, *26*(7), 2247–2267. https://doi.org/10.1175/JCLI-D-12-00150.1

Forster, P. M., Andrews, T., Good, P., Gregory, J. M., Jackson, L. S., & Zelinka, M. (2013). Evaluating adjusted forcing and model spread for historical and future scenarios in the CMIP5 generation of climate models. *Journal of Geophysical Research: Atmospheres*, *118*, 1139–1150. https://doi.org/10.1002/jgrd.50174

Frölicher, T. L., Fischer, E. M., & Gruber, N. (2018). Marine heatwaves under global warming. *Nature*, *560*(7718), 360–364. https://doi.org/10.1038/s41586-018-0383-9

Frölicher, T. L., Joos, F., Plattner, G. K., Steinacher, M., & Doney, S. C. (2009). Natural variability and anthropogenic trends in oceanic oxygen in a coupled carbon cycle-climate model ensemble. *Global Biogeochemical Cycles*, *23*, GB1003. https://doi.org/10.1029/2008GB003316

Frölicher, T. L., Rodgers, K. B., Stock, C. A., & Cheung, W. W. L. (2016). Sources of uncertainties in 21st century projections of potential ocean ecosystem stressors. *Global Biogeochemical Cycles*, *30*, 1224–1243. https://doi.org/10.1002/2015GB005338

Fu, W., Primeau, F., Keith Moore, J., Lindsay, K., & Randerson, J. T. (2018). Reversal of increasing tropical ocean hypoxia trends with sustained climate warming. *Global Biogeochemical Cycles*, *32*, 551–564. https://doi.org/10.1002/2017GB005788

Galbraith, E. D., & Jaccard, S. L. (2015). Deglacial weakening of the oceanic soft tissue pump: Global constraints from sedimentary nitrogen isotopes and oxygenation proxies. *Quaternary Science Reviews*, *109*, 38–48. https://doi.org/10.1016/j.quascirev.2014.11.012

Garcia, H. E., & Gordon, L. I. (1992). Oxygen solubility in seawater: Better fitting equations. *Limnology and Oceanography*, *37*(6), 1307–1312. https://doi.org/10.4319/lo.1992.37.6.1307

Gnanadesikan, A., Dunne, J. P., & John, J. (2012). Understanding why the volume of suboxic waters does not increase over centuries of global warming in an Earth system model. *Biogeosciences*, *9*(3), 1159–1172. https://doi.org/10.5194/bg-9-1159-2012

Griffies, S. M. (1998). The Gent–McWilliams skew flux. *Journal of Physical Oceanography*, *28*(5), 831–841. https://doi.org/10.1175/1520-0485(1998)028<0831:TGMSF>2.0.CO;2

Griffies, S. M. (2012). Elements of the modular ocean model (MOM). *GFDL Model Doc.*, *3*(C), 1–631.

Gruber, N. (2008). The marine nitrogen cycle: Overview and challenges. In D. G. Capone et al. (Eds.), *Nitrogen in the marine environment* (2nd Ed., pp. 1–50). Academic Press. https://doi.org/10.1016/B978-0-12-372522-6.00001-3, https://www.sciencedirect.com/science/article/pii/B9780123725226000013

Gruber, N. (2011). Warming up, turning sour, losing breath: Ocean biogeochemistry under global change. *Philosophical Transactions of the Royal Society A - Mathematical Physical and Engineering Sciences*, *369*(1943), 1980–1996. https://doi.org/10.1098/rsta.2011.0003

Haumann, F. A., Gruber, N., & Münnich, M. (2020). Sea-ice induced Southern Ocean subsurface warming and surface cooling in a warming climate. *AGU Advances*, *1*, e2019AV000132. https://doi.org/10.1029/2019AV000132

Helm, P., Bindoff, N., & John, C. (2011). Observed decreases in oxygen content of the global ocean. *Geophysical Research Letters*, *38*, L23602. https://doi.org/10.1029/2011GL049513

Heuzé, C. (2020). Antarctic bottom water and North Atlantic deep water in CMIP6 models. *Ocean Science Discussions*, *2020*, 1–38. https://doi.org/10.5194/os-2020-66

Heuzé, C., Heywood, K. J., Stevens, D. P., & Ridley, J. K. (2013). Southern Ocean bottom water characteristics in CMIP5 models. *Geophysical Research Letters*, *40*, 1409–1414. https://doi.org/10.1002/grl.50287

Ito, T., & Deutsch, C. (2013). Variability of the oxygen minimum zone in the tropical North Pacific during the late twentieth century. *Global Biogeochemical Cycles*, *27*, 1119–1128. https://doi.org/10.1002/2013GB004567

Ito, T., Follows, M. J., & Boyle, E. A. (2004). Is AOU a good measure of respiration in the oceans? *Geophysical Research Letters*, *31*, L17305. https://doi.org/10.1029/2004GL020900

Ito, T., Minobe, S., Long, M. C., & Deutsch, C. (2017). Upper ocean O_2 trends: 1958–2015. *Geophysical Research Letters*, *44*, 4214–4223. https://doi.org/10.1002/2017GL073613

Jaccard, S. L., & Galbraith, E. D. (2012). Large climate-driven changes of oceanic oxygen concentrations during the last deglaciation. *Nature Geoscience*, *5*(2), 151–156. https://doi.org/10.1038/ngeo1352

Jaccard, S. L., Galbraith, E. D., Frölicher, T. L., & Gruber, N. (2014). Ocean (de)oxygenation across the last deglaciation: Insights for the future. *Oceanography*, *27*, 26–35. https://doi.org/10.5670/oceanog.2014.05

Jaccard, S. L., Galbraith, E. D., Martínez-García, A., & Anderson, R. F. (2016). Covariation of deep Southern Ocean oxygenation and atmospheric CO_2 through the last ice age. *Nature*, *530*(7589), 207–210. https://doi.org/10.1038/nature16514

Keeling, R. F., Körtzinger, A., & Gruber, N. (2010). Ocean deoxygenation in a warming world. *Annual Review of Marine Science*, *2*(1), 199–229. https://doi.org/10.1146/annurev.marine.010908.163855

Killworth, P. D. (1983). Deep convection in the World Ocean. *Reviews of Geophysics*, *21*(1), 1. https://doi.org/10.1029/RG021i001p00001

Krasting, J. P., Stouffer, R. J., Griffies, S. M., Hallberg, R. W., Malyshev, S. L., Samuels, B. L., & Sentman, L. T. (2018). Role of ocean model formulation in climate response uncertainty. *Journal of Climate*, *31*(22), 9313–9333. https://doi.org/10.1175/JCLI-D-18-0035.1

Laufkötter, C., John, J. G., Stock, C. A., & Dunne, J. P. (2017). Temperature and oxygen dependence of the remineralization of organic matter. *Global Biogeochemical Cycles*, *31*, 1038–1050. https://doi.org/10.1002/2017GB005643

Laufkötter, C., Vogt, M., Gruber, N., Aita-Noguchi, M., Aumont, O., Bopp, L., et al. (2015). Drivers and uncertainties of future global marine primary production in marine ecosystem models. *Biogeosciences*, *12*(4), 3731–3824. https://doi.org/10.5194/bgd-12-3731-2015

Laufkötter, C., Vogt, M., Gruber, N., Aumont, O., Bopp, L., Doney, S. C., et al. (2016). Projected decreases in future marine export production: The role of the carbon flux through the upper ocean ecosystem. *Biogeosciences*, *13*(13), 4023–4047. https://doi.org/10.5194/bg-13-4023-2016

Levin, L. A. (2018). Emergence of open ocean deoxygenation. *Annual Review of Marine Science*, (September 2017), 1–32.

Liu, W., Xie, S.-P., Liu, Z., & Zhu, J. (2017). Overlooked possibility of a collapsed Atlantic Meridional Overturning Circulation in warming climate. *Science Advances*, *3*, e1601666. https://doi.org/10.1126/sciadv.1601666

Manabe, S., Stouffer, R. J., Spelman, M. J., & Bryan, K. (1991). Transient responses of a coupled ocean–atmosphere model to gradual changes of atmospheric CO_2. Part I. Annual mean response. *Journal of Climate*, *4*(8), 785–818. https://doi.org/10.1175/1520-0442(1991)004<0785:TROACO>2.0.CO;2

Martin, T., Park, W., & Latif, M. (2013). Multi-centennial variability controlled by Southern Ocean convection in the Kiel Climate Model. *Climate Dynamics*, *40*(7-8), 2005–2022. https://doi.org/10.1007/s00382-012-1586-7

Matear, R. J., Hirst, A. C., & McNeil, B. I. (2000). Changes in dissolved oxygen in the Southern Ocean with climate change. *Geochemistry, Geophysics, Geosystems*, *1*(11), 2000GC000086. https://doi.org/10.1029/2000GC000086

Moffitt, S. E., Hill, T. M., Roopnarine, P. D., & Kennett, J. P. (2015). Response of seafloor ecosystems to abrupt global climate change. *Proceedings of the National Academy of Sciences*, *112*, 4684–4689. https://doi.org/10.1073/pnas.1417130112

Moore, J. K., Fu, W., Primeau, F., Britten, G. L., Lindsay, K., Long, M., et al. (2018). Sustained climate warming drives declining marine biological productivity. *Science*, *359*(6380), 1139–1143.

Morrison, A. K., Griffies, S. M., Winton, M., Anderson, W. G., & Sarmiento, J. L. (2016). Mechanisms of Southern Ocean heat uptake and transport in a global eddying climate model. *Journal of Climate*, *29*(6), 2059–2075. https://doi.org/10.1175/JCLI-D-15-0579.1

Myhre, S. E., Kroeker, K. J., Hill, T. M., Roopnarine, P., & Kennett, J. P. (2017). Community benthic paleoecology from high-resolution climate records: Mollusca and foraminifera in post-glacial environments of the California margin. *Quaternary Science Reviews*, *155*, 179–197. https://doi.org/10.1016/j.quascirev.2016.11.009

Newsom, E. R., Bitz, C. M., Bryan, F. O., Abernathey, R., & Gent, P. R. (2016). Southern Ocean deep circulation and heat uptake in a high-resolution climate model. *Journal of Climate*, *29*(7), 2597–2619. https://doi.org/10.1175/JCLI-D-15-0513.1

Orsi, A. H. (2010). Oceanography: Recycling bottom waters. *Nature Geoscience*, *3*(5), 307–309. https://doi.org/10.1038/ngeo854

Oschlies, A., Brandt, P., Stramma, L., & Schmidtko, S. (2018). Drivers and mechanisms of ocean deoxygenation. *Nature Geoscience*, *11*(7), 467–473. https://doi.org/10.1038/s41561-018-0152-2

Oschlies, A., Schulz, K. G., Riebesell, U., & Schmittner, A. (2008). Simulated 21st century's increase in oceanic suboxia by CO_2-enhanced biotic carbon export. *Global Biogeochemical Cycles*, *22*, GB4008. https://doi.org/10.1029/2007GB003147

Paynter, D., Frölicher, T. L., Horowitz, L. W., & Silvers, L. G. (2018). Equilibrium climate sensitivity obtained from multimillennial runs of two GFDL climate models. *Journal of Geophysical Research: Atmospheres*, *123*, 1921–1941. https://doi.org/10.1002/2017JD027885

Plattner, G.-K., Joos, F., & Stocker, T. F. (2002). Revision of the global carbon budget due to changing air-sea oxygen fluxes. *Global Biogeochemical Cycles*, *16*(4), 1096. https://doi.org/10.1029/2001GB001746

Pörtner, H. O., Karl, D. M., Boyd, P. W., Cheung, W. W. L., Lluch-Cota, S. E., Nojiri, Y., et al. (2014). Ocean systems. *In Climate change 2014: impacts, adaptation, and vulnerability. Part A: global and sectoral aspects. contribution of working group II to the fifth assessment report of the intergovernmental panel on climate change* (pp. 411–484). Cambridge University Press.

Rayner, N. A., Parker, D. E., Horton, E. B., Folland, C. K., Alexander, L. V., Rowell, D. P., et al. (2003). Global analyses of sea surface temperature, sea ice, and night marine air temperature since the late nineteenth century. *Journal of Geophysical Research*, *108*(D14), 4407. https://doi.org/10.1029/2002JD002670

Ridgwell, A., & Schmidt, D. N. (2010). Past constraints on the vulnerability of marine calcifiers to massive carbon dioxide release. *Nature Geoscience*, *3*(3), 196–200. https://doi.org/10.1038/ngeo755

Riebesell, U., Schulz, K. G., Bellerby, R. G. J., Botros, M., Fritsche, P., Meyerhöfer, M., et al. (2007). Enhanced biological carbon consumption in a high CO_2 ocean. *Nature*, *450*(7169), 545–548. https://doi.org/10.1038/nature06267

Rugenstein, M., Bloch-Johnson, J., Abe-Ouchi, A., Andrews, T., Beyerle, U., Cao, L., et al. (2019). LongRunMIP: Motivation and design for a large collection of millennial-length AOGCM simulations. *Bulletin of the American Meteorological Society*, *100*(12), 2551–2570. https://doi.org/10.1175/BAMS-D-19-0068.1

Rugenstein, M., Bloch-Johnson, J., Gregory, J., Andrews, T., Mauritsen, T., Li, C., et al. (2020). Equilibrium climate sensitivity estimated by equilibrating climate models. *Geophysical Research Letters*, *47*, e2019GL083898. https://doi.org/10.1029/2019GL083898

Rugenstein, M. A., Sedláček, J., & Knutti, R. (2016). Nonlinearities in patterns of long-term ocean warming. *Geophysical Research Letters*, *43*, 3380–3388. https://doi.org/10.1002/2016GL068041

Russell, J. L., Dixon, K. W., Gnanadesikan, A., Stouffer, R. J., & Toggweiler, J. R. (2006). The Southern Hemisphere westerlies in a warming world: Propping open the door to the deep ocean. *Journal of Climate*, *19*(24), 6382–6390. https://doi.org/10.1175/JCLI3984.1

Sarmiento, J. L., Hughes, T. M. C., Stouffer, R. J., & Manabe, S. (1998). Simulated response of the ocean carbon cycle to anthropogenic climate warming. *Nature*, *393*(6682), 245–249. https://doi.org/10.1038/30455

Savitzky, A., & Golay, M. J. E. (1964). Smoothing and differentiation of data by simplified least squares procedures. *Analytical Chemistry*, *36*(8), 1627–1639. https://doi.org/10.1021/ac60214a047

Schmidtko, S., Stramma, L., & Visbeck, M. (2017). Decline in global oceanic oxygen content during the past five decades. *Nature*, *542*(7641), 335–339. https://doi.org/10.1038/nature21399

Schmittner, A., Oschlies, A., Matthews, D. H., & Galbraith, E. D. (2008). Future changes in climate, ocean circulation, ecosystems, and biogeochemical cycling simulated for a business-as-usual CO_2 emission scenario until Year 4000 AD. *Global Biogeochemical Cycles*, *22*, GB1013. https://doi.org/10.1029/2007GB002953

Shakun, J. D., Clark, P. U., He, F., Marcott, S. A., Mix, A. C., Liu, Z., et al. (2012). Global warming preceded by increasing carbon dioxide concentrations during the last deglaciation. *Nature*, *484*(7392), 49–54. https://doi.org/10.1038/nature10915

Skinner, L. C., Fallon, S., Waelbroeck, C., Michel, E., & Barker, S. (2010). Ventilation of the deep Southern Ocean and deglacial CO_2 rise. *Science*, *328*(5982), 1147–1151. https://doi.org/10.1126/science.1183627

Steinacher, M., Joos, F., Frölicher, T. L., Bopp, L., Cadule, P., Doney, S. C., et al. (2010). Projected 21st century decrease in marine productivity: A multi-model analysis. *Biogeosciences*, *6*(4), 7933–7981. https://doi.org/10.5194/bgd-6-7933-2009

Stendardo, I., & Gruber, N. (2012). Oxygen trends over five decades in the North Atlantic. *Journal of Geophysical Research*, *117*, C11004. https://doi.org/10.1029/2012JC007909

Stouffer, R. J., & Manabe, S. (2003). Equilibrium response of thermohaline circulation to large changes in atmospheric CO_2 concentration. *Climate Dynamics*, *20*(7-8), 759–773. https://doi.org/10.1007/s00382-002-0302-4

Stramma, L., Johnson, G. C., Sprintall, J., & Mohrholz, V. (2008). Expanding oxygen-minimum zones in the tropical oceans. *Science*, *320*(5876), 655–658. https://doi.org/10.1126/science.1153847

Stramma, L., Prince, E. D., Schmidtko, S., Luo, J., Hoolihan, J. P., Visbeck, M., et al. (2011). Expansion of oxygen minimum zones may reduce available habitat for tropical pelagic fishes. *Nature Climate Change*, *2*, 33–37.

Talley, L. D., Pickard, G. L., Emery, W. J., & Swift, J. H. (2011). Physical properties of seawater. *Descriptive physical oceanography* (pp. 29–65). Boston: Academic Press.

Thiele, G., & Sarmiento, J. L. (1990). Tracer dating and ocean ventilation. *Journal of Geophysical Research*, *95*(C6), 9377–9391. https://doi.org/10.1029/JC095iC06p09377

Vaquer-Sunyer, R., & Duarte, C. M. (2008). Thresholds of hypoxia for marine biodiversity. *Proceedings of the National Academy of Sciences of the United States of America*, *105*(40), 15,452–15,457. https://doi.org/10.1073/pnas.0803833105

Winton, M. (2000). A reformulated three-layer sea ice model. *Journal of Atmospheric and Oceanic Technology*, *17*(4), 525–531. https://doi.org/10.1175/1520-0426(2000)017<0525:ARTLSI>2.0.CO;2

Yamamoto, A., Abe-Ouchi, A., Shigemitsu, M., Oka, A., Takahashi, T., Ohgaito, R., & Yamanaka, Y. (2015). Global deep ocean oxygenation by enhanced ventilation in the Southern Ocean under long-term global warming. *Global Biogeochemical Cycles*, *29*, 1801–1815. https://doi.org/10.1002/2015GB005181

Zickfeld, K., Eby, M., Weaver, A. J., Alexander, K., Crespin, E., Edwards, N. R., et al. (2013). Long-term climate change commitment and reversibility: An EMIC intercomparison. *Journal of Climate*, *26*(16), 5782–5809. https://doi.org/10.1175/JCLI-D-12-00584.1